PCCP

ROYAL SOCIETY OF CHEMISTRY

PAPER

View Article Online
View Journal | View Issue

Cite this: *Phys. Chem. Chem. Phys.*, 2024, **26**, 13131

Size-dependent reactivity of Rh cationic clusters to reduce NO by CO in the gas phase at high temperatures†

Ken Miyajima, [a] Toshiaki Nagata, [a] Fumitaka Mafuné, *[a] Tomoya Ichino, [b] Satoshi Maeda, [bc] Taizo Yoshinaga, [d] Masahide Miura [d] and Takahiro Hayashi [d]

Received 1st December 2023,
Accepted 5th April 2024

DOI: 10.1039/d3cp05862j

rsc.li/pccp

The reactivity of the reduction of NO pre-adsorbed on Rh_{2-9}^+ clusters by CO was investigated using a combination of an alternate on–off gas injection method and thermal desorption spectrometry. The reduction of $Rh_nN_xO_y^+$ clusters by CO was evaluated by varying the CO concentration at T = 903 K. Among the $Rh_nN_xO_x^+$ clusters, the $Rh_3N_2O_2^+$ cluster exhibited the highest reduction activity, whereas the other clusters, $Rh_{2,4-9}N_xO_x^+$, showed lower reactivity. Density functional theory (DFT) calculations for Rh_3^+ and Rh_6^+ revealed that the rate-determining step for NO reduction in the presence of CO was NO bond dissociation through the kinetics analysis using the RRKM theory. The reduction of $Rh_3N_2O_2^+$ is kinetically preferable to that of $Rh_6N_2O_2^+$. The DFT results were in qualitative agreement with the experimental results.

1. Introduction

Among all precious metals, rhodium has the highest significance in reducing hazardous nitric oxide gas in automobile exhaust.[1] Many studies have attempted to understand and improve the efficiency of catalytic activity involving extended Rh surfaces.[2–9] Gas-phase clusters are an ideal model to evaluate chemical reactivity and compare them with theoretical calculations, as the number of atoms involved in the reactions is well defined.[10–12] NO decomposition on $Rh_n^{+/-}$ clusters has been investigated extensively.[13–17] Mackenzie *et al.* reported NO decomposition on small charged rhodium clusters observed using a Fourier transform ion cyclotron resonance mass spectrometer.[12–14] They found size-dependent trends in the reaction mechanism and efficiency of NO decomposition. For small clusters (n = 7–16), once two NO molecules are coadsorbed on a cluster, N_2 is evolved, generating the corresponding oxide cluster.[15] Hirabayashi and Ichihashi studied the effect of doping with a second metal (Al, V, or Co) on the NO reactivity of small Rh cluster cations.[17] They examined the reactions of Rh_5X^+ (X = Al, V, Co, and Rh) with NO under multiple-collision conditions and observed the cluster dioxide formation and N_2 release. In particular, V doping was the most effective for NO decomposition.

An important step in the catalytic reaction is the rupture of the N–O bond. Indeed, the release of the N_2 molecule from $Rh_nN_xO_x^+$ requires the NO molecule to dissociate, forming two or more N atoms, which then migrate to form an N–N bond.[18] The presence of the N–O bond in the NO-attached Rh metal clusters was observed using vibrational spectroscopy.[19,20] When Rh metal clusters react with NO gas, the prominent products obtained are $Rh_n(NO)_m^+$.[18] Note that this notation does not indicate that the NO molecule retains the N–O bond after adsorption on the rhodium cluster. In the case of Rh_6^+ clusters, the first NO molecule is molecularly adsorbed onto an on-top site of the octahedral skeleton.[19] The second NO molecule adsorbs either molecularly on another on-top site or dissociates into N and O atoms in a ratio of approximately 1 : 0.4.

In contrast to the N atoms, the O atoms, resulting from NO bond dissociation, bind much more strongly to the Rh cluster.[21,22] Therefore, the oxidation of CO by the O atom is an essential step for completing the catalytic cycle. Recently, Chen *et al.* reported a catalytic cycle for the conversion of NO

[a] *Department of Basic Science, Graduate School of Arts and Sciences, The University of Tokyo, Komaba, Meguro-ku, Tokyo 153-8902, Japan. E-mail: mafune@cluster.c.u-tokyo.ac.jp*
[b] *Institute for Chemical Reaction Design and Discovery (WPI-ICReDD), Hokkaido University, N21-W10, Kita-ku, Sapporo, Hokkaido 001-0021, Japan*
[c] *Department of Chemistry, Faculty of Science, Hokkaido University, N10-W8, Kita-ku, Sapporo, Hokkaido 060-0810, Japan*
[d] *Advanced Material Engineering Division, Toyota Motor Corporation, 1200, Mishuku, Susono, Shizuoka 410-1193, Japan*

† Electronic supplementary information (ESI) available: Mass spectra of $Rh_{2-10}N_xO_y^+$ at 303 K, 663 K, and 903 K; signal intensity of $Rh_{2-7}N_xO_y^+$ cluster ions after heating in an extension tube at 903 K; TDS plots for n = 3 with alternate on–off gas injection of CO; TDS plots for $Rh_{2-5}N_xO_y^+$; entire free energy profiles for the reduction of $Rh_3N_2O_2^+$ and $Rh_6N_2O_2^+$ by CO; octahedral structures at transition states for NO dissociation and CO oxidation; optimized structures and energies. See DOI: https://doi.org/10.1039/d3cp05862j

and CO into N_2 and CO_2, mediated by gas-phase neutral rhodium–aluminum oxide clusters.[12] They observed the oxidation of CO by $RhAlO_{0-3}$ and $RhAl_2O_{1-4}$ clusters after single-photon ionization using VUV light (118 nm, 10.5 eV). Previous studies on rhodium metal clusters have shown a size dependence of the reaction rate.[15,18] Information regarding the temperature dependence of the reaction is essential for further understanding. Therefore, it is important to analyze the reactivity of clusters under high-temperature conditions using mass spectrometry.

In this study, we investigated the size dependence of the reactivity of NO reduction by CO on Rh clusters that pre-reacted with NO under multi-collision conditions. The thermal desorption of NO and/or N_2 from $Rh_nN_xO_y^+$ clusters and their CO reactivity were evaluated by alternate on–off gas injection of CO.[23] The observed difference in CO reactivity between $Rh_3N_2O_2^+$ and $Rh_6N_2O_2^+$ was explained using density functional theory (DFT) calculations.

2. Methods

2.1. Experimental methods

The reduction of NO by CO on Rh_n^+ clusters under thermalized conditions at high temperatures was investigated using an alternate on–off CO gas injection method developed by our group in combination with thermal desorption spectrometry (TDS) (Fig. 1).[23] Gas-phase clusters were prepared by laser ablation of a rhodium metal rod using a focused second harmonic (532 nm; 10 Hz) of a Nd:YAG pulse laser at a typical pulse energy of 10 mJ. The Rh metal atoms were then cooled in an NO-seeded He gas flow (He purity > 99.99995%; NO concentration 0.017%) from a solenoid pulse valve (General Valve; stagnation pressure 0.65 MPa) to form $Rh_nN_xO_y^+$. A slush bath made from ethanol and liquid nitrogen was used to trap impurities (N_2O, NO_2, and H_2O) in the carrier gas.[24] Here, the number of N atoms, x, was assumed to be the same as the number of O atoms, y, because NO molecules were adsorbed onto Rh_n^+. However, few O-rich clusters ($y > x$) were generated,[18] likely because of the pre-oxidation of the Rh rod surface. The mass flow and pressure controllers maintained the NO concentration at the desired level.

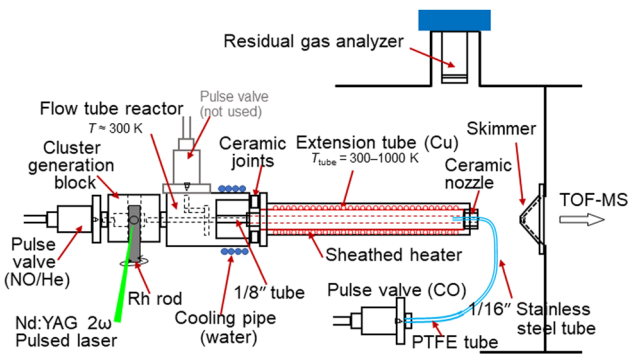

Fig. 1 Experimental setup of the alternate on–off CO gas injection method developed by our group in combination with TDS.

$Rh_nN_xO_y^+$ clusters prepared in the carrier gas were introduced into an extension tube before expansion in a vacuum chamber. The tube was heated to 300–1000 K using a resistive heater and the temperature was monitored using type-K thermocouples. The residence time of the cluster ions and the density of the He gas in the extension tube were estimated to be approximately 100 μs and 10^{18} molecules cm^{-3}, respectively. In the tube, the clusters were heated through collisions with the surrounding He gas, which was considered to have achieved thermal equilibrium.[25] The reactant CO gas was injected from the nozzle through a pulse valve near the end of the extension tube at a stagnation pressure of 530 Torr to ensure that the heated clusters reacted with CO. The volume of the CO gas pulse was adjusted based on the duration of the pulse valve and the time delay, achieving both a significant mass spectral change and sufficient signal intensity. The CO gas injection was alternated by turning it on for 600 shots (corresponding to two mass spectra) and off for 900 shots (three mass spectra) while the temperature was adjusted for the TDS measurement. This asymmetric alternation of the reactant gas injection displays a clear distinction in the TDS plot. A residual gas analyzer (RGA; MKS e-Vision2) was used to monitor the volumes of NO and CO introduced into the vacuum chamber through the valves. When measuring the CO concentration dependence, the CO concentration in the mixed gas was controlled by scanning the flow rates of the CO and He gases using two mass flow controllers and removing the excess gas using a pressure controller to maintain a constant pressure.

The product ions, which were expanded in a vacuum, were accelerated by a pulsed electric field to gain a kinetic energy of 3.5 keV using a time-of-flight spectrometer for mass analysis. The ions were detected using a Hamamatsu double-microchannel plate detector after passing through a 1 m field-free flight tube. The signals were amplified using a preamplifier and digitized using an oscilloscope. Each mass spectrum was obtained by accumulating signals for 300 shots. The mass resolution was sufficiently high ($m/\Delta m > 1000$ at $m/z = 1000$) to distinguish the Rh, C, N, and O atoms in the mass spectra.

2.2. Computational methods

Systematic calculations were performed using the artificial force induced reaction (AFIR) method, as implemented in the GRRM program, to search for cluster structures and reaction pathways.[26] The calculations were performed using the DFT method with the TURBOMOLE program package.[27] For the reactant, intermediate, and product states, the local minima were searched using the single component AFIR (SC-AFIR) method with the model collision energy parameter γ = 100 kJ mol^{-1}. The NO dissociation and CO oxidation paths were searched starting from the obtained dissociative adsorption structures using the SC-AFIR method and applying an artificial force between N and O and between O and C, respectively, with γ = 1000 kJ mol^{-1}. All the obtained AFIR paths were re-optimized using the in-house modified locally updated plane (LUP) path optimization method.[28] The highest energy points along the LUP paths (the approximate TSs), except those higher than 20 kJ mol^{-1} above the lowest

approximate TS, were optimized to the true TSs. Path connections were confirmed using intrinsic reaction coordinate (IRC) calculations. Structure optimization and IRC calculations were performed without any geometric constraints. The DFT calculations were performed at the PBE/def2-SV(P) level using the RI-J technique.[29–31] During the search calculations, the lowest spin states were targeted and identified using the Fermi option of the TURBOMOLE program. The same procedure was used in our previous work on transition metal hexamer-assisted bond activation.[32]

For small Rh clusters, the TPSSh functional provided accurate geometries and reaction energies with respect to the experimental results.[33] Therefore, the low-lying reactant, intermediate, product, and transition-state structures in the PBE results were further optimized at the TPSSh-D3/def2-SV(P) level of theory using the RI-J technique.[34,35] In these calculations, the lowest spin states were manually identified based on a comparison with the calculations for a wide range of spin states. Normal mode analysis was performed on all of the optimized structures. Finally, single-point energy calculations were performed at the TPSSh-D3/def2-TZVP level of theory using the RI-JK technique (TPSSh-D3/def2-TZVP//def2-SV(P)).[36] Rate constants based on the Rice–Ramsperger–Kassel–Marcus (RRKM) theory[37–41] were evaluated to validate the thermalization of intermediates in the reaction pathway through comparison with the collision rate of He gas. Gibbs free energy values under the experimental conditions (903 K and 0.04 atm) were also computed.

3. Results

3.1. Mass spectra of $Rh_nN_xO_y^+$ clusters with and without CO gas reactions

Fig. 2a shows the mass spectrum focusing on the n = 3 mass region of the nascent $Rh_nN_xO_y^+$ cluster ions generated by the adsorption of NO on the Rh clusters at 303 K. The ion peaks assigned to $Rh_3N_4O_4^+$, $Rh_3N_5O_5^+$, $Rh_3N_6O_6^+$, $Rh_3N_6O_7^+$, and $Rh_3N_7O_7^+$ were observed in the spectrum. After heating the extension tube to 903 K, the ion peaks shifted to lower masses in the spectrum, which were mainly assigned to Rh_3NO^+, $Rh_3N_2O_2^+$, and $Rh_3N_3O_4^+$ (Fig. 2b). Mass spectra of the whole region are shown in Fig. S1–S3 (ESI†). It is speculated that the NO molecules adsorbed at 300 K were desorbed from the clusters when they were heated. Upon introduction of CO gas into the extension tube at 903 K, peaks assignable to Rh_3^+, Rh_3N^+, Rh_3NO^+, $Rh_3N_2O^+$, and $Rh_3N_2O_2^+$ appeared. The intensities of Rh_3NO^+ and $Rh_3N_2O_2^+$ decreased, whereas those of Rh_3N^+ and, most prominently, $Rh_3N_2O^+$ increased. These findings suggest that the CO molecules extract O atoms from Rh_3NO^+ and $Rh_3N_2O_2^+$ to form CO_2. This pair of increased and decreased compositions observed for n = 3 in response to the removal of one oxygen atom by CO was also clear for n = 4 and weaker for n = 5 and 6 (Fig. S6, ESI†).

3.2. Thermal desorption and alternate on–off gas injection of CO

3.2.1. CO reactivity of $Rh_3N_xO_y^+$. The relative intensities of $Rh_3N_xO_y^+$ were measured as a function of the temperature in the extension tube (TDS plot; Fig. 3). The cluster ions were grouped with the same $y - x$ value ($y - x$ = +1 to −6) and are shown from top to bottom. The intensity changes of the clusters were caused by the heat and/or reactions with CO in the extension tube. By alternate on–off gas injection of CO, the intensities of specific clusters changed accordingly, which provided comb-like response signals in the plots.

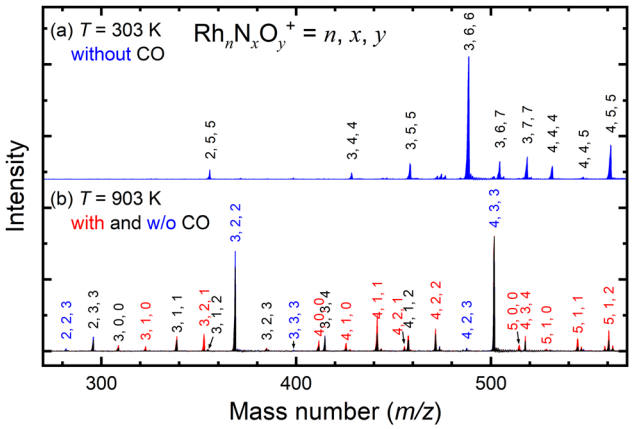

Fig. 2 (a) Mass spectrum of nascent $Rh_3N_xO_y^+$ cluster ions generated by the adsorption reactions of NO on Rh clusters at 303 K. (b) Mass spectrum after heating in an extension tube at 903 K. The blue line corresponds to the case of no reaction with CO and the red line corresponds to the reaction with CO. The area filled in black is the area that appeared in both cases. Clusters with increased/decreased intensities due to CO are indicated by red and blue labels, respectively.

First, let us examine the reactions caused by heat by examining the data points depicted by filled circles corresponding to the reactions in the absence of CO. At 303 K, $Rh_3N_6O_6^+$ was dominant. A small amount of $Rh_3N_7O_7^+$ present at room temperature quickly disappeared upon heating. The intensity of $Rh_3N_6O_6^+$ gradually decreased with increasing temperature from 400 to 500 K, which was accompanied by an increase in the intensity of $Rh_3N_4O_4^+$ before $Rh_3N_5O_5^+$ gained intensity. Subsequently, the intensity of $Rh_3N_4O_4^+$ decreased above 650 K, and the intensity of $Rh_3N_2O_2^+$ increased rapidly before that of $Rh_3N_3O_3^+$. In addition, the intensity of $Rh_3N_2O_2^+$ decreased at temperatures above 850 K, whereas that of Rh_3NO^+ increased. The changes in the ion intensities can be explained by NO desorption from the clusters by heat. The apparent N_2O_2 loss can be attributed to the binding energy of NO release. Presumably, the binding energy of an NO molecule in $Rh_3N_5O_5^+$ is lower than that of the binding energy in $Rh_3N_6O_6^+$, and the binding energy of an NO molecule in $Rh_3N_3O_3^+$ is lower than that of the binding energy in $Rh_3N_4O_4^+$. When the clusters were heated to a sufficiently high temperature to allow the NO molecule in $Rh_3N_6O_6^+$ to be readily released from $Rh_3N_6O_6^+$, the less weakly bound NO molecule in $Rh_3N_5O_5^+$ was released simultaneously, resulting in the indistinctive appearance of the peaks for $Rh_3N_5O_5^+$ and $Rh_3N_3O_3^+$. However, the activation energies of NO desorption estimated by fitting were, as expected, lower for $Rh_3N_5O_5^+$ than for $Rh_3N_6O_6^+$ but much higher for $Rh_3N_3O_3^+$ than for $Rh_3N_4O_4^+$. The TDS curve observed in the experiment was better reproduced by adding a reaction channel that desorbs two NO molecules at a time to the model in which

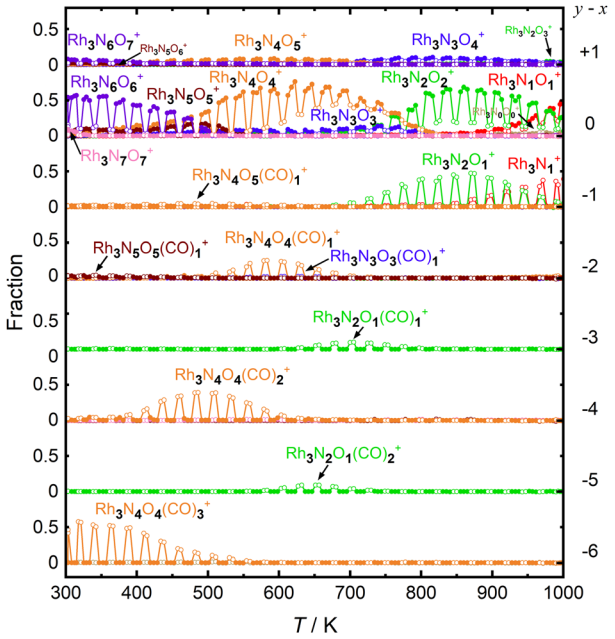

Fig. 3 TDS plots with alternate on–off gas injection of CO for n = 3 in the temperature range of 300–1000 K. Cluster ions, $Rh_3N_xO_y^+$, grouped with the same $y - x$ value ($y - x$ = +1 – –6), are shown from top to bottom. Even when a CO molecule is presumed to be originally attached, our mass resolution cannot distinguish it from two N atoms attached. Here, for the purpose of plotting in one figure, a cluster with k CO molecules attached is categorized as if the cluster had 2k N atoms instead of the k CO molecules. The intensities in the presence and absence of CO are depicted by the open and filled circles, respectively. The number of N atoms in the cluster is color-coded as red, green, blue, orange, brown, purple, and pink.

one NO molecule is desorbed at a time. This suggests that there may also be a pathway in which NO is desorbed as an NO dimer.[42] Other pairs of compositions, such as $Rh_4N_8O_8^+$ and $Rh_4N_5O_5^+$, $Rh_5N_8O_8^+$ and $Rh_5N_6O_6^+$, and $Rh_6N_7O_7^+$ and $Rh_6N_5O_5^+$ showed desorption between intermediate compositions with low relative intensities similar to this one. In such cases, NO may also be released as a dimer, rather than as a single molecule.

At 400–600 K, the O-rich cluster ion $Rh_3N_4O_5^+$ appeared, although the intensity was low and decreased further at temperatures above 650 K. $Rh_3N_3O_4^+$ and $Rh_3N_2O_3^+$ appeared at 800 and 900 K, respectively. Based on these intensity changes, concomitant changes in the reactant and product cluster pairs were observed. NO molecules were sequentially released from the clusters on heating, as shown in the following reaction scheme:

$$Rh_3N_xO_x^+ \rightarrow Rh_3N_{x-1}O_{x-1}^+ + NO \quad (x = 2\text{–}6), \qquad (1)$$

$$Rh_3N_xO_{x+1}^+ \rightarrow Rh_3N_{x-1}O_x^+ + NO \quad (x = 3\text{–}6). \qquad (2)$$

Additionally, the data points in Fig. 3 with open circles show the intensities of the clusters when the CO gas was turned on. At 300–700 K, the intensity of $Rh_3N_6O_6^+$ decreased and that of $Rh_3N_4O_4(CO)_3^+$ increased when the CO gas was on. A detailed examination of the mass spectrum revealed that when CO gas was added, a group of peaks with compositions in which NO was gradually replaced by CO, for example, from $Rh_5N_9O_9^+$ to $Rh_5N_6O_6(CO)_3^+$, appeared because of the ligand exchange reaction (Fig. S1, ESI†). These changes became insignificant above 550 K. It should be noted that the mass numbers of $Rh_3N_4O_4(CO)_3^+$ (m/z = 512.69) were approximately the same as those of $Rh_3N_6O_4(CO)_2^+$ (m/z = 512.70), $Rh_3N_8O_4(CO)^+$ (m/z = 512.72), and $Rh_3N_{10}O_4^+$ (m/z = 512.73), and the species could not be identified uniquely by the current mass resolution. Nevertheless, we can assign the mass peak to CO-adsorbed species, such as $Rh_3N_6O_4(CO)_2^+$ and $Rh_3N_4O_4(CO)_3^+$, because the intensity of $Rh_3N_6O_6^+$ decreases when CO is turned on. It is difficult to discern the reason for the occurrence of the reactions by increasing the number of N atoms in the clusters, given that the reaction counterpart was CO. There is a strong possibility that O_2 or NO was replaced by CO. In addition, the intensity of $Rh_3N_4O_4^+$ decreased and that of $Rh_3N_4O_4(CO)_2^+$ increased when CO gas was turned on at temperatures above 400 K. Therefore, the intensity changes were speculated to be caused by the adsorption of CO molecules on $Rh_3N_4O_4^+$ *via* the following reaction:

$$Rh_3N_4O_4^+ + 2CO \rightarrow Rh_3N_4O_4(CO)_2^+. \qquad (3)$$

The adsorption of CO was observed only below 750 K, as CO desorption from the clusters accelerated above 700 K. Above 700 K, the intensity of $Rh_3N_2O_2^+$ decreased and the intensity of $Rh_3N_2O^+$ increased when CO gas was turned on. In addition, above 850 K, when Rh_3NO^+ was generated by thermal desorption, the intensity of Rh_3NO^+ decreased and that of Rh_3N^+ increased when the CO gas was turned on. The loss of O atoms by reaction with CO can be explained by the reduction by CO to form CO_2. For O-rich clusters, $Rh_3N_2O_3^+$, $Rh_3N_3O_4^+$, and $Rh_3N_4O_5^+$ also decreased when the CO gas was turned on. Hence, it can be inferred that the reduction reaction of the clusters occurred *via*

$$Rh_3N_xO_{x+1}^+ + CO \rightarrow Rh_3N_xO_x^+ + CO_2 \quad (x = 2, 3, 4), \qquad (4)$$

$$Rh_3N_xO_x^+ + CO \rightarrow Rh_3N_xO_{x-1}^+ + CO_2 \quad (x = 1, 2). \qquad (5)$$

3.2.2. CO reactivity of $Rh_{2-6}N_xO_y^+$. The same analysis as that for the $Rh_3N_xO_y^+$ case was performed for the $Rh_{2,4,5,6}N_xO_y^+$ cases, and the TDS plots for the clusters above 600 K are shown in Fig. S6 (ESI†). As shown in eqn (1) and (2), it can be seen that the observed intensities of $Rh_nN_xO_x^+$ and $Rh_nN_xO_{x+1}^+$ proceed with heating, respectively, with the desorption of NO with strong and weak intensities. On the other hand, focusing on the modulation of the curve shape by CO on–off, we see that the reduction of $Rh_nN_xO_x^+$ and $Rh_nN_xO_{x+1}^+$ clusters by CO occurs, as shown in eqn (4) and (5).

For comparison, Fig. 4 shows the selected fractions of one-O-atom-deficient clusters, $Rh_nN_xO_{x-1}^+$ (n = 2–6), along with the main products of the reduction reaction by CO as a function of temperature. The reaction schemes for n = 4–6 are similar to those for n = 3, although the reactivities of the reductions by CO are much lower than those for n = 3. Thus, the reduction reactivity of CO displayed a considerable size dependence.

3.3. Concentration dependence of CO at 903 K: size dependence

Fig. 5 shows the fraction of $Rh_nN_xO_y^+$ clusters produced for each value of n as a function of CO concentration. The temperature of

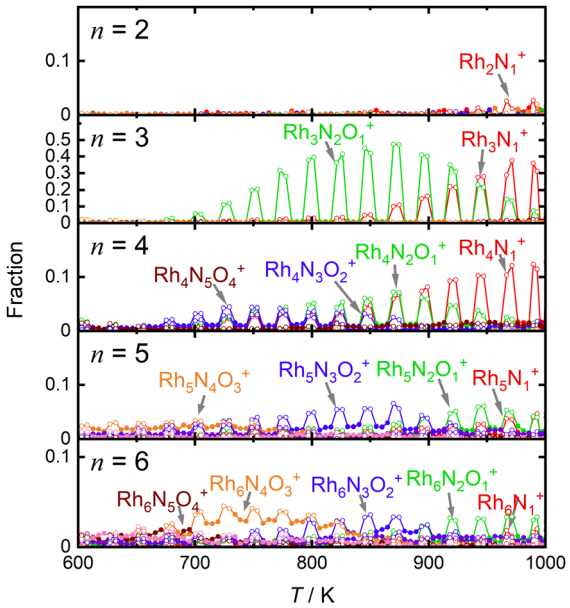

Fig. 4 Intensity changes of one-O-atom-deficient $Rh_nN_xO_{x-1}^+$ (n = 2–6), the main products of the reduction reaction by CO, as a function of temperature in the range of 600–1000 K. Intensities in the presence and absence of CO are depicted by open and filled circles, respectively. The number of N atoms in the cluster is color-coded as red, green, blue, orange, brown, purple, and pink.

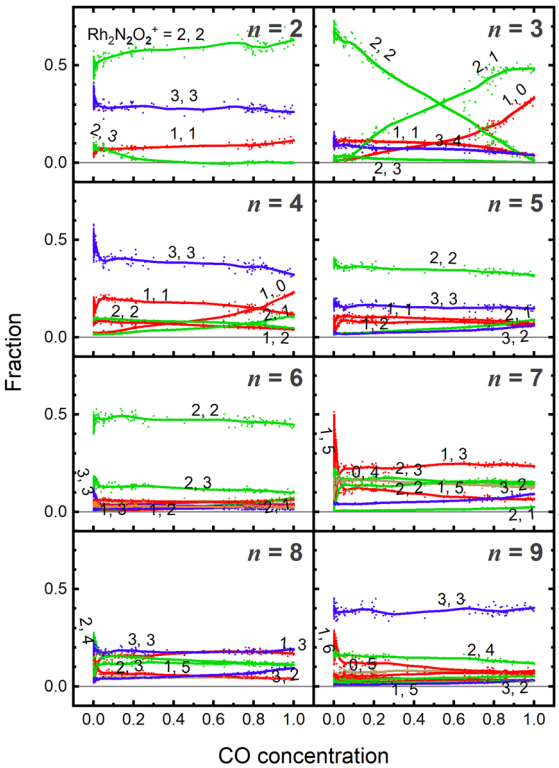

Fig. 5 Fractions of $Rh_nN_xO_y^+$ clusters (n = 2–9) produced by the reaction of CO at 903 K as a function of CO concentration. Lines in the plots were added for visibility. The colors khaki, red, green, and blue correspond to compositions containing zero, one, two, and three N atoms, respectively.

the extension tube was set at 903 K, and the concentration of the reactant, CO, was gradually varied. The fraction of $Rh_3N_2O_2^+$ decreased significantly with increasing CO concentration, whereas that of $Rh_3N_2O^+$ and Rh_3N^+ increased. Rh_3NO^+ also decreased; however, the decrease was smaller than the increase in Rh_3N^+, suggesting that there was a formation path for Rh_3N^+ other than the direct abstraction of the O atom from Rh_3NO^+. Based on the fraction balance, Rh_3N^+ is considered to be produced from $Rh_3N_2O_2^+$ simultaneously *via* reduction by CO and desorption of NO. For n = 2, $Rh_2N_2O_3^+$ decreases and $Rh_2N_2O_2^+$ increases with increasing CO concentration; however, no other clear changes are observed.

4. Discussion

4.1. Thermal desorption of NO and reduction by CO

Based on the experimental results, a reaction scheme for the thermal desorption of NO and reduction of $Rh_3N_xO_y^+$ by CO is presented in Scheme 1. $Rh_3N_xO_x^+$ and one-O-atom-rich $Rh_3N_xO_{x+1}^+$, generated at low temperatures, formed Rh_3N^+ above 900 K in the presence of CO. The reaction schemes for n = 4 and 5 are similar to that for n = 3.

For n = 7 and 8, several O-rich clusters, including $Rh_7NO_3^+$, $Rh_7NO_5^+$, $Rh_7O_4^+$, $Rh_8NO_3^+$, $Rh_8NO_5^+$, and $Rh_8N_2O_4^+$, were produced by thermal desorption in the absence of CO, which is consistent with our previous study.[18] These O-rich clusters were formed by N_2 released from $Rh_7N_xO_x^+$ and $Rh_8N_xO_x^+$. We expected that these clusters would be effectively reduced by CO, forming clusters with fewer O atoms and increasing the N-rich clusters. However, the oxygen-rich clusters $Rh_7NO_5^+$, $Rh_8NO_5^+$, and $Rh_9NO_6^+$ were rapidly depleted in the low CO concentration region, as shown in Fig. 5. The pair of decrease and increase in intensity induced by mixing CO may have induced the following oxygen release reactions:

$$Rh_7NO_5^+ + CO \rightarrow Rh_7NO_3^+ + CO + O_2 \quad (6)$$

After showing an abrupt change in the low-concentration region, no change in the intensity was observed with increasing CO concentration. This may be due to the presence of a certain percentage of less reactive isomers. In the experimental setup, we observed reactions within the extension tube with a residence time of ~100 μs. Conceivably, more time is required to observe further reactions.

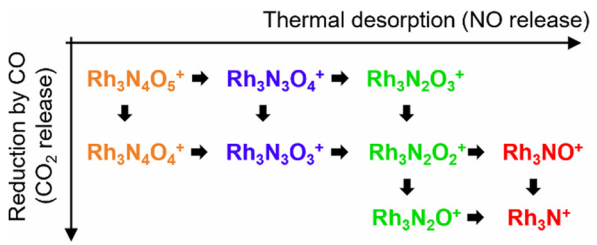

Scheme 1 Schematic representation of the reaction pathway of $Rh_3N_xO_y^+$ clusters.

4.2. Size and composition dependence of the reactivity of reduction by CO

As previously mentioned, the reduction reactivity of CO is size dependent. The fractions of the clusters for n = 6–9 varied slightly as the CO concentration increased, indicating that they were less reactive for reduction by CO. To understand the size and composition dependence of reactivity, the relative rate constant $k_{rel}(n, x, y)$ of the reduction reaction of $Rh_nN_xO_y^+$ was calculated by assuming a pseudo-first-order reaction between CO at T = 903 K.

In this experiment, because cluster ions were not mass-selected, the intensities of multiple clusters changed concurrently because of the reaction with CO. The rate constants for the selected clusters were estimated by analyzing the concentration dependence, as shown in Fig. 5 and summarized in Fig. 6. Generally, the rate constants for oxygen-rich clusters, $Rh_nN_xO_{x+1}^+$, are larger than those for the corresponding $Rh_nN_xO_x^+$ clusters. In particular, $Rh_2N_2O_3^+$, which contains excess oxygen, exhibited the highest reaction rate observed in this study. This cluster is considered to be reduced by the following reaction:

$$Rh_2N_2O_3^+ + CO \rightarrow Rh_2N_2O_2^+ + CO_2 \quad (7)$$

The clusters produced by the above equation did not undergo further reduction with CO under the present conditions. The rate constant for the $Rh_nN_xO_x^+$ clusters was low at n = 2, highest at n = 3, and decreased with increasing n. Thus, the reactivity for n = 3 is markedly higher than that of the other clusters. This observation is contrary to intuitive expectations given that larger clusters have more open surface sites than smaller clusters. DFT calculations were performed to clarify the differences between $Rh_3N_2O_2^+$ and $Rh_6N_2O_2^+$ clusters.

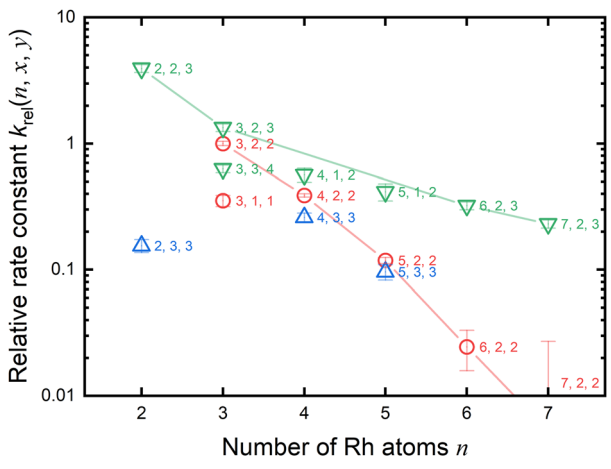

Fig. 6 Relative rate constant $k_{rel}(n, x, y)$ of the reduction reaction of $Rh_nN_xO_y^+$ at 903 K was estimated by measuring the decreasing rate of the fraction of $Rh_{3-7}N_2O_2^+$, $Rh_{2,4}N_3O_3^+$, and $Rh_nN_xO_{x+1}^+$ with the CO concentration for each n. Rate constants were normalized to that of $Rh_3N_2O_2^+$. Red circles, blue triangles, and green triangles correspond to $Rh_nN_2O_2^+$, $Rh_nN_3O_3^+$, and $Rh_nN_xO_{x+1}^+$, respectively. To indicate the size-dependence of $Rh_nN_2O_{2,3}^+$, the lines are shown as a guide.

4.3. Quantum chemical calculation of reaction paths

Fig. 5 and 6 show that the cluster with $Rh_3N_2O_2^+$ exhibited the highest reduction activity, whereas the clusters with $Rh_{6-9}N_xO_x^+$ exhibited lower reactivity. To investigate the observed size dependency, we performed theoretical calculations on the reactivity of n = 3 and n = 6 clusters. Using DFT in combination with a systematic pathway search method, we calculated the geometrical structures and energy barriers of the reactions of $Rh_3N_2O_2^+$ and $Rh_6N_2O_2^+$ with CO.

Fig. 7 shows the zero-point corrected energy profiles and structural changes in the NO dissociation and CO oxidation steps involved in the reduction of $Rh_3N_2O_2^+$ and $Rh_6N_2O_2^+$ by CO. The complete energy profile, including adsorbate migration and Rh cluster shape changes, is shown in Fig. S7 (ESI†) for n = 3 and Fig. S8 (ESI†) for n = 6. For the reactions of n = 3 and n = 6, two reaction mechanisms are proposed based on the difference in the order of dissociation of the NO molecules and adsorption of CO: (1) two NO molecules, which adsorb molecularly on Rh_3^+ or Rh_6^+ (RCTa), dissociate (INT1), followed by CO adsorption (INT2). (2) It is also possible that NO dissociation occurred after the co-adsorption of the two NOs and CO (RCTb). In both cases, a single O-deficient cluster (PRD) is generated by CO_2 formation and desorption.

Bare Rh_3^+ and Rh_6^+ clusters exhibit triangular and octahedral geometries, respectively. As shown in Fig. 7a, the Rh_3 cluster retains its triangular geometry throughout RCT, INT, PRD, and TS. In contrast, the Rh_6 cluster retained its octahedral geometry at RCT, INT, and PRD, while forming different geometries at TS1a/b and TS2. In particular, the Rh_6 structures at TS1a/b and TS2 correspond to metastable isomers, namely capped square pyramid and boat structures, respectively, which have been considered in spectroscopic and DFT studies for the gas-phase Rh_6^+ cluster.[43] It is worth noting that the octahedral structures at TS1a/b and TS2 are less stable than the lowest energy TS structures by 0.46, 1.00, and 0.31 eV, respectively (Fig. S9, ESI†). A previous study on transition metal hexamer-assisted bond activation highlighted the importance of metastable cluster structures in assisting bond activation.[32] The active sites for NO dissociation and CO_2 formation were identified at the hollow site for n = 3 and the 4-fold hollow site for n = 6. In particular, the active sites for NO dissociation at n = 6 are similar to those on the Rh(100) surface.[7,44]

For n = 3, the NO bond dissociation step with/without CO adsorption is endothermic by 0.07/0.18 eV with an activation energy of 0.94/1.11 eV. The CO oxidation step is also endothermic by 0.34 eV with an activation energy of 0.79 eV. For n = 6, the NO dissociation step with/without CO adsorption is exothermic by −1.17/−0.63 eV with an activation energy of 0.39/0.92 eV, while the CO oxidation step is endothermic by 1.50 eV with an activation energy of 1.64 eV. It should be noted that for n = 6, the actual activation energy for NO dissociation with CO adsorption is 0.85 eV (Fig. S8, ESI†), and this may be attributed to the presence of another high barrier that causes a shape change of the Rh_6 moiety before NO dissociation. However, this value is still smaller than the activation energy of 1.64 eV for CO oxidation. In short, NO dissociation and CO oxidation are endothermic/exothermic

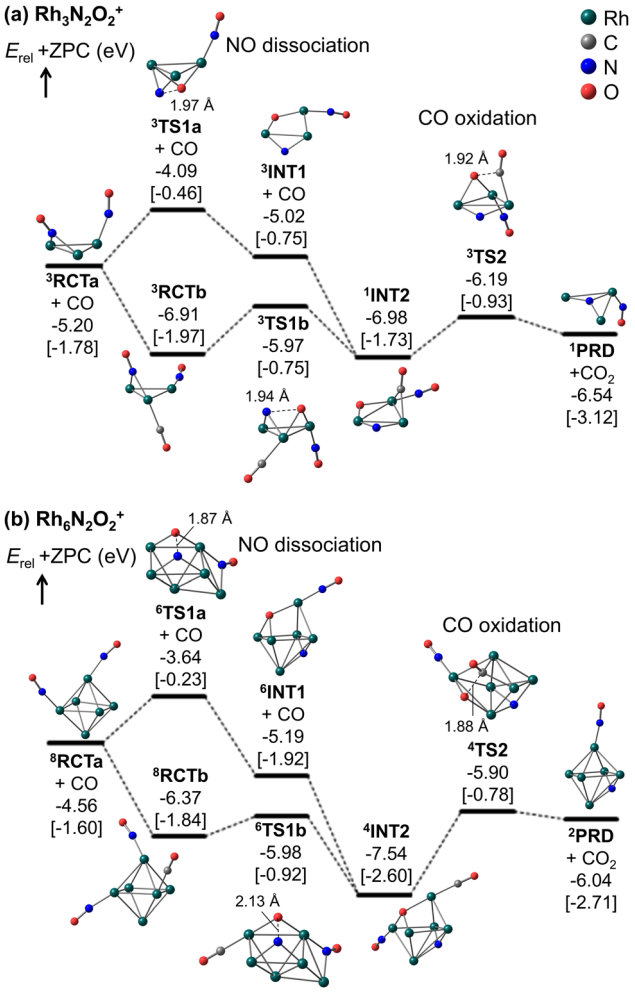

Fig. 7 Zero-point corrected energy profiles of the reduction reactions of (a) $Rh_3N_2O_2^+$ and (b) $Rh_6N_2O_2^+$ by CO, calculated at the TPSSh-D3/def2-TZVP//def2-SV(P) level of theory using the RI technique. The cluster structures correspond to the lowest energy structures at the reactant RCT, intermediate INT, product PRD, and transition state TS for NO dissociation and CO oxidation processes. Superscripts on the labels indicate spin multiplicity. The energy levels are expressed relative to the sum of the energies of the bare Rh cluster, 2NO, and CO. Relative Gibbs free energy (T = 903 K, P = 0.04 atm) is additionally shown in square brackets.

and endothermic/endothermic, respectively, for n = 3/6. The RRKM rate constants for the NO dissociation and CO oxidation steps, with the total energy of the reactants (electronic energy plus zero-point energy) as the total energy, are estimated to be 4.7×10^{10} and 7.5×10^{11} s^{-1} for n = 3, and 1.6×10^9 and 5.0×10^9 s^{-1} for n = 6, revealing that the reduction for n = 3 is kinetically preferable to that for n = 6. Furthermore, NO bond dissociation was identified as the rate-determining step for both sizes. Comparing to the collision rate of He (around 10^9 s^{-1}), the structural changes of intermediates could proceed with higher frequency than the collision with He. It is, thus, considered that the clusters might not reach thermal equilibrium in the extension tube. The $Rh_{3,6}(NO)_2(CO)^+$ clusters could generate CO_2 with the larger excess energy during the residence time of approximately 100 μs. A simple kinetic analysis of the reaction profiles presented in Fig. S7 and S8 in the ESI,† based on the rate constant matrix construction method,[45] shows that the ratio of $k_{rel}(n, x, y)$ is (3, 2, 2) : (6, 2, 2) = 1 : 0.03. Thus, our DFT results are in qualitative agreement with the experimental results for the rate constant ratio, as shown in Fig. 6.

According to Fig. 7, the N–Rh_6–O moiety in INT1 and INT2 for n = 6 represents the lowest-energy dissociatively adsorbed structures, which are identified by both spectroscopic and DFT methods.[19] In these structures, the N and O atoms are adsorbed at different hollow sites in the octahedral Rh_6 motif. Conversely, in the N–Rh_3–O moiety, the N and O atoms were adsorbed on different edge sites of the triangular Rh_3 motif because of the presence of only a single hollow site for adsorption, and were not sufficiently stabilized. The site-specific binding energies of the N and O atoms were strongly correlated with the relative stabilities of the dissociatively adsorbed states.[21] The stabilization energy caused by dissociative adsorption increased with the binding energies of the N and O atoms. In addition, Fig. 7 shows that as NO dissociation becomes more exothermic, the NO dissociation barrier decreases, and the CO oxidation barrier increases. Thus, the relative stability of the dissociatively adsorbed states would be involved in the difference in the reactivity between $Rh_3N_2O_2^+$ and $Rh_6N_2O_2^+$.

In particular, for n = 6, the order (10^9 s^{-1}) of RRKM rate constants for the NO dissociation and CO oxidation steps could be comparable to the collision frequency of He gas. These collision rates may be influenced by the CO concentration in the tube. Therefore, the kinetics of n = 6 should be carefully investigated with both rate constants based on the RRKM theory and transition state theory. If the collision frequency decreases slightly because of the higher CO concentration, the cluster ions might not achieve thermal equilibrium, leading to the active $Rh_6(NO)_2(CO)^+$ species generate CO_2, as mentioned above. On the other hand, if the collision frequency increases slightly under a lower CO concentration, the cluster ions might be thermalized. From the free energy evaluation, shown in Fig. 7b, the CO oxidation from ^{4}INT2 (1.82 eV and 1.31×10^3 s^{-1}) is identified as a rate-determining step, revealing that the intermediate cannot get over the barrier within the residence time. These discussions might relate with the observed fraction change of $Rh_6N_2O_1^+$ in Fig. 5.

5. Conclusions

The size-dependent reactivities of rhodium oxynitride clusters, $Rh_nN_xO_y^+$ (n = 2–9), and carbon monoxide were studied by gas-phase thermal desorption spectrometry using the alternate on–off gas injection method. The loss of O atoms from the reaction with CO can be explained by the reduction by CO, which resulted in the formation of CO_2. The rate constants for the $Rh_nN_xO_x^+$ cluster and CO were approximately zero at n = 2, were highest at n = 3, and decreased with n. DFT calculations of the geometrical structures and energy barriers for the reactions of $Rh_3N_2O_2^+$ and $Rh_6N_2O_2^+$ with CO revealed that NO bond dissociation is identified to be a rate-determining step through the

evaluation of RRKM rate constants. From comparing the order of the rate constants, the reduction for n = 3 is kinetically preferable to that for n = 6. In addition, the DFT results were in qualitative agreement with the experimental results for the relative rate constant.

Author contributions

K. M.: conceptualization, methodology, investigation, software, visualization, writing – original draft and writing – review & editing; T. N.: writing – review & editing; F. M.: conceptualization, writing – review & editing, project administration and funding acquisition; T. I.: investigation, visualization, writing – original draft and writing – review & editing; S. M.: project administration and funding acquisition; T. Y.: project administration and funding acquisition; M. M.: writing – review & editing; T. H.: writing – review & editing.

Conflicts of interest

There are no conflicts to declare.

Acknowledgements

The authors would like to thank Dr. Satoshi Kudoh for quantum calculations on the $Rh_3N_xO_y^+$ and $Rh_6N_xO_y^+$ clusters in the early stages of this work.

References

1 H. Hirata, Recent research progress in automotive exhaust gas purification catalyst, *Catal. Surv. Asia*, 2014, **18**, 128–133.
2 D. G. Castner, B. A. Sexton and G. A. Somorjai, LEED and thermal desorption studies of small molecules (H_2, O_2, CO, CO_2, NO, C_2H_4, C_2H_2 and C) chemisorbed on the rhodium (111) and (100) surfaces, *Surf. Sci.*, 1978, **71**(3), 519–540.
3 C.-T. Kao, G. S. Blackman, M. A. Van Hove, G. A. Somorjai and C.-M. Chan, The surface structure and chemical reactivity of Rh(111)-(2 × 2)-3NO by HREELS and dynamical LEED analysis, *Surf. Sci.*, 1989, **224**, 77–96.
4 J. S. Villarrubia and W. Ho, Nitric oxide adsorption, decomposition, and desorption on Rh(100), *J. Chem. Phys.*, 1987, **87**, 750–764.
5 A. G. Makeev and M. M. Slinko, Mathematic modelling of the peculiarities of NO decomposition on Rh(111), *Surf. Sci.*, 1996, **359**, L467–L472.
6 F. Zaera and C. S. Gopinath, Role of adsorbed nitrogen in the catalytic reduction of NO on rhodium surfaces, *J. Chem. Phys.*, 1999, **111**, 8088–8097.
7 D. Loffreda, F. Delbecq, D. Simon and P. Sautet, Breaking the NO bond on Rh, Pd, and Pd_3Mn alloy (100) surfaces: A quantum chemical comparison of reaction paths, *J. Chem. Phys.*, 2001, **115**, 8101–8111.
8 T. Hirai, M. Okoshi, A. Ishikawa and H. Nakai, Temperature- and pressure-dependent adsorption configuration of NO molecules on Rh(111) surface: A theoretical study, *Surf. Sci.*, 2019, **686**, 58–62.
9 A. Ishikawa and Y. Tateyama, First-principles microkinetic analysis of NO + CO reactions on Rh(111) surface toward understanding NO_x reduction pathways, *J. Phys. Chem. C*, 2018, **122**, 17378–17388.
10 S. M. Lang and T. M. Bernhardt, Gas phase metal cluster model systems for heterogeneous catalysis, *Phys. Chem. Chem. Phys.*, 2012, **14**, 9255–9269.
11 Y. X. Zhao, X. G. Zhao, Y. Yang, M. Ruan and S. G. He, Rhodium chemistry: A gas phase cluster study, *J. Chem. Phys.*, 2021, **154**, 180901.
12 J.-J. Chen, X.-N. Li, L.-H. Mou, Q.-Y. Liu and S.-G. He, Catalytic Conversion of NO and CO into N_2 and CO_2 by Rhodium–aluminum oxides in the gas phase, *J. Mater. Chem. A*, 2021, **10**, 6031–6037.
13 Y. Tawaraya, S. Kudoh, K. Miyajima and F. Mafuné, Thermal desorption and reaction of NO adsorbed on rhodium cluster ions studied by thermal desorption spectroscopy, *J. Phys. Chem. A*, 2015, **119**, 8461–8468.
14 M. S. Ford, M. L. Anderson, M. P. Barrow, D. P. Woodruff, T. Drewello, P. J. Derrick and S. R. Mackenzie, Reactions of nitric oxide on Rh_6^+ clusters: Abundant chemistry and evidence of structural isomers, *Phys. Chem. Chem. Phys.*, 2005, **7**, 975–980.
15 M. L. Anderson, M. S. Ford, P. J. Derrick, T. Drewello, D. P. Woodruff and S. R. Mackenzie, Nitric oxide decomposition on small rhodium clusters, $Rh_n^{+/-}$, *J. Phys. Chem. A*, 2006, **110**, 10992–11000.
16 D. Harding, S. R. Mackenzie and T. R. Walsh, Structural isomers and reactivity for Rh_6 and Rh_6^+, *J. Phys. Chem. B*, 2006, **110**, 18272–18277.
17 S. Hirabayashi and M. Ichihashi, Effects of second-metal (Al, V, Co) doping on the NO reactivity of small rhodium cluster cations, *J. Phys. Chem. A*, 2017, **121**, 2545–2551.
18 T. Nagata, K. Kawada, X. Chen, M. Yamaguchi, K. Miyajima and F. Mafuné, Decomposition of nitric oxide by rhodium cluster cations at high temperatures, *Phys. Chem. Chem. Phys.*, 2021, **23**, 26721.
19 T. Nagata, S. Kudoh, K. Miyajima, J. M. Bakker and F. Mafuné, Adsorption of multiple NO molecules on Rh_n^+ (n = 6, 7) investigated by infrared multiple photon dissociation spectroscopy, *J. Phys. Chem. C*, 2018, **122**, 22884–22891.
20 T. Nagata, K. Koyama, S. Kudoh, K. Miyajima, J. M. Bakker and F. Mafuné, Adsorption forms of NO on Rh_n^+ (n = 6–16) revealed by infrared multiple photon dissociation spectroscopy, *J. Phys. Chem. C*, 2017, **121**, 27417–27426.
21 M. Yamaguchi, S. Kudoh, K. Miyajima, O. V. Lushchikova, J. M. Bakker and F. Mafuné, Tuning the dissociative action of cationic Rh clusters toward NO by substituting a single Ta atom, *J. Phys. Chem. C*, 2019, **123**, 3476–3481.
22 M. Yamaguchi, Y. Zhang, S. Kudoh, K. Koyama, O. V. Lushchikova, J. M. Bakker and F. Mafuné, Oxophilicity as a descriptor for NO cleavage efficiency over group IX metal clusters, *J. Phys. Chem. Lett.*, 2020, **11**, 4408–4412.
23 X. Chen, K. Miyajima and F. Mafuné, Newly-developed alternate on–off gas injection method for investigation of

reduction of gas-phase cobalt oxide clusters by CO at high temperature, *Chem. Phys. Lett.*, 2022, **792**, 139418.
24 R. E. Rondeau, Slush Baths, *J. Chem. Eng. Data*, 2002, **11**, 124–124.
25 T. Nagata, K. Miyajima and F. Mafuné, Stable stoichiometry of gas-phase cerium oxide cluster ions and their reactions with CO, *J. Phys. Chem. A*, 2015, **119**, 1813–1819.
26 S. Maeda, Y. Harabuchi, M. Takagi, K. Saita, K. Suzuki, T. Ichino, Y. Sumiya, K. Sugiyama and Y. Ono, Implementation and performance of the artificial force induced reaction method in the GRRM17 Program, *J. Comput. Chem.*, 2018, **39**, 233–250.
27 R. Ahlrichs, M. K. Armbruster, R. A. Bachorz, H. Bahmann, A. Baldes, M. Bär, H.–P. Baron, R. Bauernschmitt, F. A. Bischoff, S. Böcker, A. M. Burow, N. Crawford, P. Deglmann, F. D. Sala, M. Diedenhofen, M. Ehrig, K. Eichkorn, S. Elliott, Y. J. Franzke, D. Friese, F. Furche, T. Gimon, A. Glöß, N. Graf, L. Grajciar, F. Haase, M. Häser, C. Hättig, A. Hellweg, B. Helmich, S. Höfener, C. Holzer, H. Horn, C. Huber, W. Hujo, U. Huniar, M. Kattannek, S. Klawohn, W. Klopper, A. Köhn, C. Kölmel, M. Kollwitz, K. Krause, M. Kühn, R. Łazarski, T. M. Maier, F. Mack, K. May, N. Middendorf, P. Nava, C. Ochsenfeld, H. Öhm, M. Pabst, H. Patzelt, P. Pollak, D. Rappoport, K. Reiter, O. Rubner, A. Schäfer, G. Schmitz, U. Schneider, T. Schwabe, M. Sierka, D. P. Tew, O. Treutler, B. Unterreiner, M. von Arnim, F. Weigend, P. Weis, H. Weiss, N. Winter, *TURBOMOLE* **V7.3** 2018, a Development of University of Karlsruhe and Forschungszentrum Karlsruhe GmbH, 1989–2007, TURBOMOLE GmbH, 2007.
28 C. Choi and R. Elber, Reaction path study of helix formation in tetrapeptides: Effect of side chains, *J. Chem. Phys.*, 1991, **94**, 751–760.
29 J. P. Perdew, K. Burke and M. Ernzerhof, Generalized gradient approximation made simple, *Phys. Rev. Lett.*, 1996, **77**, 3865–3868.
30 F. Weigend and R. Ahlrichs, Balanced basis sets of split valence, triple zeta valence and quadruple zeta valence quality for H to Rn: Design and assessment of accuracy, *Phys. Chem. Chem. Phys.*, 2005, **7**, 3297–3305.
31 K. Eichkorn, O. Treutler, H. Öhm, M. Häser and R. Ahlrichs, Auxiliary basis sets to approximate Coulomb potentials, *Chem. Phys. Lett.*, 1995, **240**, 283–290.
32 T. Ichino, M. Takagi and S. Maeda, A systematic study on bond activation energies of NO, N_2, and O_2 on hexamers of eight transition metals, *ChemCatChem*, 2019, **11**, 1346–1353.
33 S. M. Hamilton, W. S. Hopkins, D. J. Harding, T. R. Walsh, M. Haertelt, C. Kerpal, P. Gruene, G. Meijer, A. Fielicke and S. R. Mackenzie, Infrared-induced reactivity of N_2O on small gas-phase rhodium clusters, *J. Phys. Chem. A*, 2011, **115**, 2489–2497.
34 V. N. Staroverov, G. E. Scuseria, J. Tao and J. P. Perdew, Comparative assessment of a new nonempirical density functional: Molecules and hydrogen-bonded complexes, *J. Chem. Phys.*, 2003, **119**, 12129–12137.
35 S. Grimme, J. Antony, S. Ehrlich and H. Krieg, A consistent and accurate ab initio parametrization of density functional dispersion correction (DFT-D) for the 94 elements H-Pu, *J. Chem. Phys.*, 2010, **132**, 154104.
36 F. Weigend, A fully direct RI-HF algorithm: Implementation, optimised auxiliary basis sets, demonstration of accuracy and efficiency, *Phys. Chem. Chem. Phys.*, 2002, **4**, 4285–4291.
37 O. K. Rice and H. C. Ramsperger, Theories of unimolecular gas reactions at low pressures. II, *J. Am. Chem. Soc.*, 1928, **50**, 617–620.
38 L. S. Kassel, Studies in homogeneous gas reactions II Introduction of quantum theory, *J. Phys. Chem.*, 1928, **32**, 1065–1079.
39 R. A. Marcus and O. K. Rice, Session on free radicals The kinetics of the recombination of methyl radical and iodine atoms, *J. Phys. Colloid Chem.*, 1951, **55**, 894–908.
40 R. A. Marcus, Unimolecular dissociations and free radical recombination reactions, *J. Phys. Chem.*, 1952, **20**, 359–364.
41 G. Z. Whitten and B. S. Rabinovitch, Accurate and facile approximation for vibrational energy level sums, *J. Chem. Phys.*, 1963, **38**, 2466–2473.
42 G. Meizyte, P. A. J. Pearcy, P. D. Watson, E. I. Brewer, A. E. Green, M. Doll, O. A. Duda and S. R. Mackenzie, An infrared study of gas-phase metal nitrosyl ion–molecule complexes, *J. Phys. Chem. A*, 2022, **126**, 9414–9422.
43 D. J. Harding, P. Gruene, M. Haertelt, G. Meijer, A. Fielicke, S. M. Hamilton, W. S. Hopkins, S. R. Mackenzie, S. P. Neville and T. R. Walsh, Probing the structures of gas-phase rhodium cluster cations by far-infrared spectroscopy, *J. Chem. Phys.*, 2010, **133**, 214304.
44 K. Tian, X.-Y. Tu and S.-S. Dai, NO dissociation pathways on Rh(1 0 0), (1 1 0), and (1 1 1) surfaces: A comparative density functional theory study, *Surf. Sci.*, 2007, **601**, 3186–3195.
45 Y. Sumiya, Y. Nagahata, T. Komatsuzaki, T. Taketsugu and S. Maeda, Kinetic analysis for the multistep profiles of organic reactions: Significance of the conformational entropy on the rate constants of the Claisen rearrangement, *J. Phys. Chem. A*, 2015, **119**, 11641–11649.